

A 9 μA , Addressable Gen2 Sensor Tag for Biosignal Acquisition

Daniel Yeager, *Student Member, IEEE*, Fan Zhang, *Student Member, IEEE*, Azin Zarrasvand, *Student Member, IEEE*, Nicole T. George, Thomas Daniel, and Brian P. Otis, *Senior Member, IEEE*

Abstract—Biosensors present exciting opportunities in novel medical and scientific applications. However, sensor tags presented to date cannot interface with practical sensors, lack addressability, and/or require a custom (high-cost) interrogator. Our tag provides these features via ultra-low-power circuitry including a low-noise biosignal amplifier, unique tag ID generator, calibration-free 3 MHz oscillator, and EPC C1 Gen2 protocol compatibility. In addition to design details and measurement data from the fabricated IC, we present *in vivo* muscle temperature measurement from an untethered in-flight hawkmoth.

Index Terms—Biomedical, implantable electronics, RFID, low power, analog.

I. INTRODUCTION

COMPELLING applications in both the scientific and medical monitoring of biosignals have created a demand for wireless, unobtrusive sensors to collect this data. Example biosignals include temperature, blood pressure, heart rate, blood glucose level, and neural activity. In scientific applications, measurement of these biosignals helps researchers study complex biological systems, the effect of various diseases, and research treatments. In clinical settings, these signals are used by a doctor or patient to either detect disease at onset or help administer treatment.

Measurement of biosignals presents several challenges. Most importantly, the sensor must be unobtrusive to the user. This involves minimizing the size and weight of the sensor as well as maximizing the sensor lifespan. A means of wireless data collection is necessary for scientific research, where data should be available in real-time, and for implantable medical biosensors where data is otherwise inaccessible. A number of solutions have been proposed including use of a small battery to power the sensor or an inductive link to power and communicate with the sensor. Unfortunately, battery-powered sensors suffer

Manuscript received April 23, 2010; revised July 10, 2010; accepted July 17, 2010. Date of current version September 24, 2010. This paper was approved by Associate Editor Kenneth Shepard. This work was supported by the National Science Foundation ECS Award 0824265, the Komen Endowed Chair, the Office of Naval Research (ONR) MURI grant to T. Daniel, and Intel Labs Seattle.

D. Yeager, F. Zhang, and B. Otis are with the Department of Electrical Engineering, University of Washington, Seattle, WA 98195 USA e-mail: (yeagerd@gmail.com; http://wireless.ee.washington.edu).

A. Zarrasvand was with the Department of Electrical Engineering, University of Washington, Seattle, WA 98195 USA, and is now with the Microelectronics Department, Raytheon Corporation, Andover, MA 01810 USA.

N. George and T. Daniel are with the Department of Biology, University of Washington, Seattle, WA 98195 USA.

Color versions of one or more of the figures in this paper are available online at <http://ieeexplore.ieee.org>.

Digital Object Identifier 10.1109/JSSC.2010.2063930

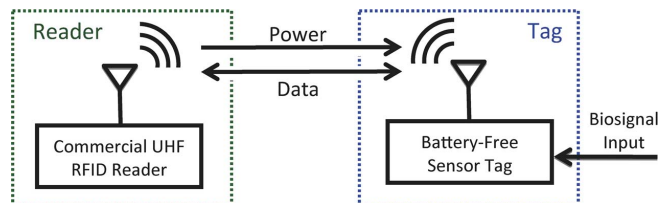


Fig. 1. Biosignal acquisition system.

from short lifespan due to the size and weight constraints of the battery. Inductively-coupled devices suffer from short wireless range (on the order of cm).

We propose the use of passive radio frequency identification (RFID) technology to address many of the challenges of biosignal sensors. Most importantly, passive RFID allows wireless, battery-free operation at meter ranges (see Fig. 1). This enables wearable and implantable biosensors with an unlimited lifespan, small size, and sub-gram weight. Many passive sensor tags reported to date have employed simple ring oscillator temperature sensors with no protocol or addressability. However, realistic applications demand accurate processing of μV -level biosignals and compatibility with industry standard RFID protocols.

We present a fully-passive 900 MHz RFID tag IC with addressability, full EPC Class 1 Generation 2 (Gen2) protocol compatibility, a $1.25 \mu\text{V}_{\text{rms}}$ integrated noise chopper-stabilized micropower sensor interface amplifier, and an 8b ADC. The communication range is 3 m with an off-the-shelf RFID reader, enabling previously impossible recording scenarios like in-flight recording from small insects. A significant improvement in performance beyond the state-of-the-art was achieved by utilizing a novel self-calibrating on-chip frequency reference, subthreshold digital logic, a low-noise chopper amplifier, 8b ADC, and a unique chip ID generator.

II. PRIOR WORK

A plethora of RFID-related research has appeared in the literature, predominately since Karthaus' [1] influential and widely-cited paper in 2003. The recent technological feasibility of RFID, coupled with numerous application spaces and widespread commercial adoption, have galvanized academic research in this field. A number of full tag implementations have been presented in the literature, and they are grouped by feature set in Table I.

TABLE I
COMPARISON OF PUBLISHED TAG FEATURES

Type	Author	Protocol	NVM	ID	Sensors	Passive
A	This Work	G2	-	Y	8b ADC	Y
A	Sample [2]	G2 ^a	Y	Y	10b ADC	Y
B	Kim [24]	G2 ^b	Y	Y	Temp	N
B	Kocer [22]	N	-	3b	5b ADC	N
C	Nakamoto [32]	ISO	Y	Y	-	Y
C	Pillai [33]	ISO	Y	Y	-	Y
C	Karthaus [1]	ISO ^c	Y	Y	-	Y
C	Barnett [25]	G2	Y	Y	-	Y
D	Shen [23]	N	-	N	8b ADC	Y
D	Cho [34]	N	-	N	Temp	Y
D	Shenghua [35]	N	-	N	Temp	Y

^aPartial protocol support

^bSensor data not sent by Gen2 protocol

^cSpecific protocol not stated in publication

A. Passive Tags With Sensors

The first category, which describes this work, represents fully-passive tags with sensors, addressability, and Gen2-compliant protocol. This combination of features enables practical deployment because (a) low-cost COTS (commercial, off-the-shelf) readers can be used, (b) sensor data can be associated with the person or animal that the tag is attached to, and (c) useful signals can be amplified, digitized and retrieved from the sensor. Although [2] includes all of the required features for a biosensor tag, its use of a commercial microcontroller requires duty cycling to satisfy its high power requirements. This significantly reduces the data rate as the wireless range increases.

B. Tags With Batteries

The second category comprises tags with batteries. These tags lack the key advantage of an RFID solution: they are limited by battery life. Furthermore, batteries add cost, weight, and safety concerns to realistic biosensing scenarios.

C. Tags Lacking Sensors

The third category includes tags with addressability but no sensors. These tags target conventional RFID applications and provide a useful design reference for the rectifier and communication circuitry.

D. Tags Lacking Addressability

The last category includes tags with sensors but no protocol/addressability. It is unclear how one would deploy this type of tag because without an ID, the sensor data they report cannot be associated with the object to which the tag is attached. Furthermore, none of these tags include an ADC to digitize practical biosignals and are thus limited in their application.

E. Tag Components

In this section, we describe prior research in components necessary for a Gen2-compatible RFID tag.

1) *Oscillators*: Gen2 RFID tags require a local oscillator to clock the digital core. In particular, the tag backscatter specifications necessitate either a precise 1.28 MHz clock or a higher clock rate with a programmable divider. Most designs employ a current-starved ring oscillator, and efforts focus on reducing variation and power consumption. Ring oscillators suffer from high sensitivity to supply voltage, bias current, temperature, mismatch, parasitics, and process variation. Several oscillators with frequencies ranging from 1 MHz to 2 MHz have been presented, however, they all require manual trimming to achieve the precision required by the EPC protocol [3], [4]. Other works suffer from poor performance or excessively high frequency, which in turn increases the digital core power consumption [5], [6]. We demonstrate in Section IV-F that an ultra-low-power tag clock can be synthesized via a ring oscillator, without trimming or tuning, by using a programmable divider and timing in the EPC protocol.

2) *Communication Logic*: Minimizing the power consumption of each tag circuit block, including the digital core that implements the tag's communication protocol, is critical in achieving high tag sensitivity. Zalbide *et al.* [7] present simulation results comparing performance gains from various power reduction strategies for a Gen2 digital core. Unfortunately, they target just one allowable link frequency and consequently may not work with commercial readers (which also only support certain subsets of the protocol). Ricci *et al.* [8] present simulation results for a 2 μ W Gen2 digital core with cryptography, and some analysis on clock frequency selection. They target a 2.0 MHz clock frequency, which cannot be guaranteed by the tag oscillator over process and temperature variation.

3) *Rectifiers*: There have been a number of in-depth analyses of UHF and microwave rectifier design. Much of the literature focuses on optimization of conventional Dickson charge pumps (voltage-doubling ladders) [9]–[12]. Mandal and Sarpeshkar [13] discuss fundamental physical relationships that link the operating bandwidth and range to technology dependent quantities like threshold voltage and parasitic capacitances. Several papers have investigated non-conventional topologies. For example, Nakamoto *et al.* [14] tune transistor V_t to maximize rectifier power conversion, achieving 36.6% efficiency. This work is replicated using floating gate pMOS transistors while optimizing for sensitivity instead of efficiency [15]. They achieve the best results to date: 1 V output voltage is reported at -22.5 dBm input power. This work is similar to patented “adaptive silicon” technology which uses floating gate V_t tuning [16].

III. SYSTEM ARCHITECTURE

The system architecture is shown in Fig. 2. One of the challenges of this work is the integration of sensitive instrumentation amplification onto a severely power-constrained platform that also suffers from tremendous supply voltage fluctuations and electromagnetic interference (EMI). Accurate signal amplification and digitization require precise supply and reference voltages. Ultra-low-power linear regulators, bandgap reference and bias current generation provide a stable bias and supply for the the chip (Section IV). Sensor input signals

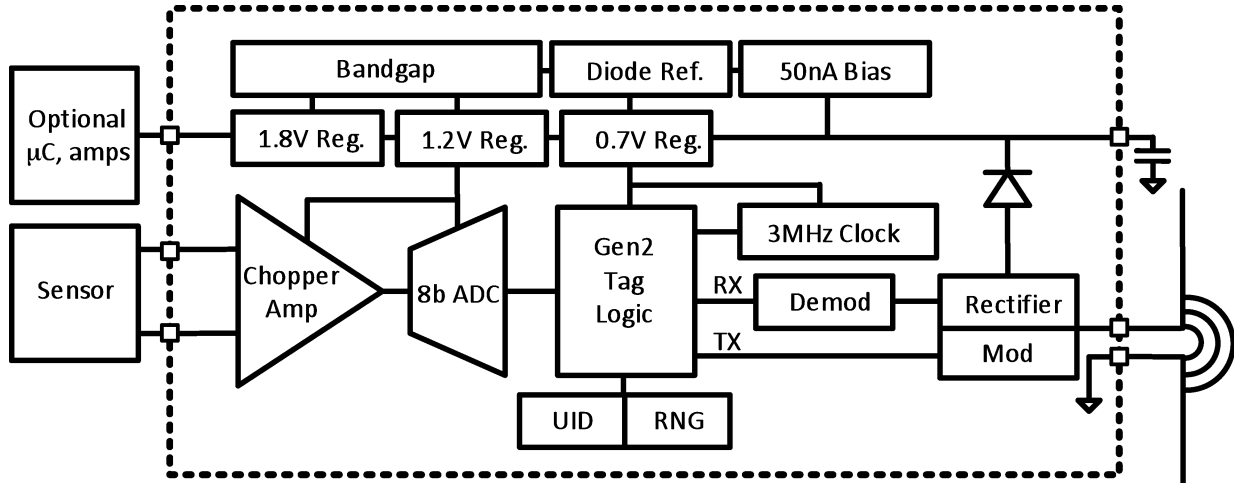


Fig. 2. Block diagram of the system.

(e.g., EEG, EMG, thermocouple) are first amplified with the on-chip low-noise chopper-stabilized amplifier (Section V). An 8b SAR ADC then digitizes the sensor data. The sensor data is associated with a person or animal by means of a unique tag ID (UID). This UID leverages process variation in the startup configuration of an SRAM, thus eliminating the need for non-volatile memory [17]. Random numbers (RN) are required in the Gen2 protocol for anticollision and (weak) encryption of reader-to-tag data. These are generated by sampling the (unpredictable) clock phase at the downlink baseband edges and passing it through an LFSR. Finally, the on-chip controller logic encodes the RN, UID, and ADC data into a Gen2-compatible packet in response to reader commands (Query/ReqRN, Ack, and Read, respectively) (Section VI). The UID and sensor data are available for real-time use by a PC through an ethernet connection to the reader.

IV. ANALOG CORE

The analog core is responsible for generating accurate bias currents and voltages for the chip, which in turn enables accurate biosignal amplification and digitization. Total measured power consumption for the analog blocks is $1.2 \mu\text{A}$. The various circuit blocks are described in the following subsections:

A. Rectifier

The RF rectifier employs a 6-stage voltage-doubling charge pump topology. High sensitivity and efficiency are achieved by using zero- V_t diode-connected nMOS devices. Measured performance is plotted in Fig. 3. An off-chip L-match network transforms the impedance to 50Ω ; alternately, this matching network can be easily absorbed into the antenna as in commercial designs.

B. Bias Current Generation

Bias currents for the chip are generated by a $45 \text{ nA } V_{gs}/R$ reference, shown in Fig. 4. Despite the use of thick-oxide devices (which allow up to 3.6 V unregulated supply voltage), the bias generator starts reliably at 0.6 V. The high output impedance of the cascode devices maintains a constant output current of 45 nA

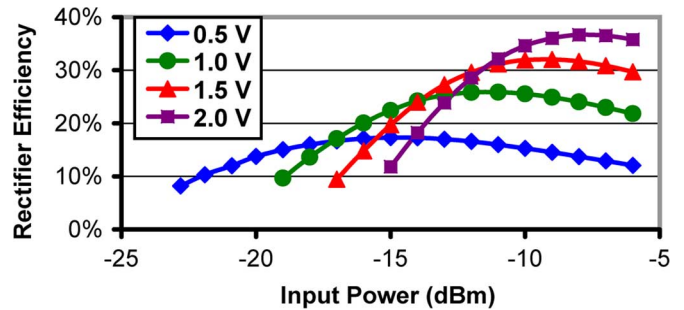


Fig. 3. Measured rectifier efficiency versus output voltage and input power.

from 0.6 V to 3.6 V as shown in Fig. 5(a). Process and mismatch variation is minimized through use of relatively-large device sizes as well as precision resistors. Simulated Monte Carlo variation is 2.8 nA (6%) without trimming [see Fig. 5(b)]. Measured bias current consumption for the full analog core corresponded well with the anticipated current based on simulation of the bias current reference.

Many startup circuits for bias current references consume significant static current. The startup circuit shown in Fig. 4 uses MOS-bipolar pseudo-resistors (M2, M3) as an area-efficient means of creating very large resistances (e.g., $>100 \text{ G}\Omega$), which minimize static current. A 200 fF capacitor provides fast transient startup when the circuit is powered on and prevents oscillation of the startup circuitry. In addition, supply noise will not cause disturbances in steady-state operation because the gates of M5 and M7 are pulled to ground. Transistors M1, M2, and M4 ensure that the gates of M5 and M7 are fully discharged in spite of off-resistance variation across process corners.

C. Bandgap Reference and Supply Regulation

A stable reference voltage is obtained through an ultra-low-power bandgap reference, shown in Fig. 6(a). The total supply current is 220 nA, and the measured output voltage is stable to within 4 mV of the nominal 1.2 V across 0–100 °C.

Three low-drop-out linear regulators provide stable supplies for the 0.7 V digital core, the 1.2 V analog core, and an auxiliary 1.8 V supply for any off-chip ICs, respectively. The 1.2 V and

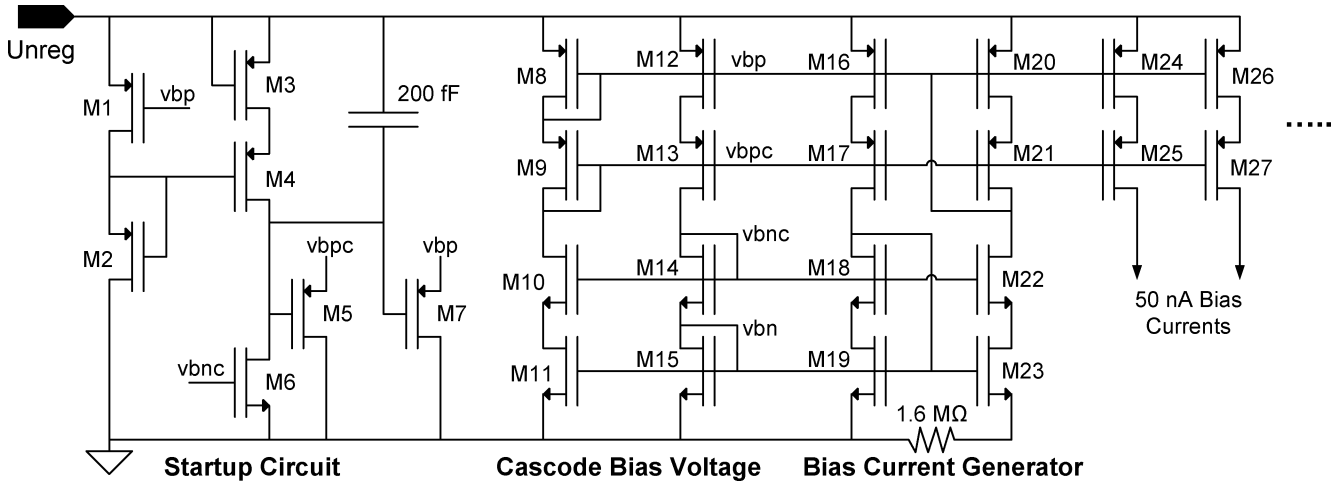


Fig. 4. Bias current generator schematic.

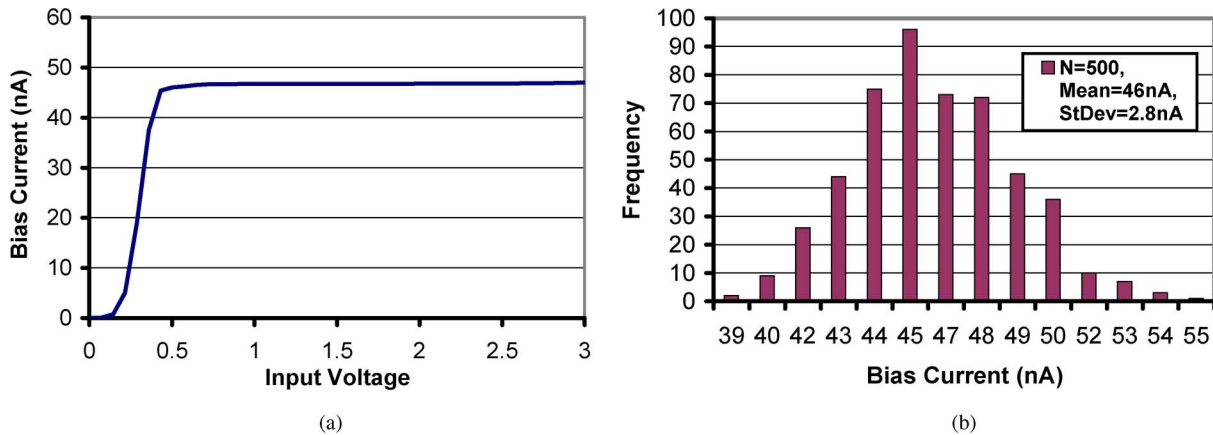


Fig. 5. Bias current generator performance. (a) Simulated bias current versus supply voltage. (b) Simulated Monte Carlo bias current distribution (process and mismatch).

1.8 V regulators utilize the bandgap voltage reference voltage, which provides a precise, temperature-independent voltage reference for the biosignal amplifier and ADC. The 0.7 V regulator is generated by sensing the transistor V_t . This creates a CTAT supply voltage that automatically compensates for process and temperature variation in the digital blocks.

The regulators employ a straightforward single-stage op-amp with 60 dB gain and 100 nA current consumption. The 0.7 V and 1.2 V regulators use unity-gain feedback, while the 1.8 V uses resistive feedback. On-chip mega-ohm resistors are used in 1.8 V regulator feedback network to limit the quiescent current. Low precision (but well-matched) resistors can be afforded because the ratio, not the absolute value, of two resistors sets the accuracy of the output voltage.

D. Demodulator

Reader-to-tag communication employs pulse-interval encoding (PIE). Specifically, the duration of the positive pulsewidth determines whether each bit is a zero or one. Positive pulses are delineated by a short negative pulse of duration

PW, which is as small as 1.66 μs . This sets the lower limit on the demodulator bandwidth to approximately 1.2 MHz.

The digital core measures and converts the positive pulse durations into data and clock. However, the received signal (the output of the rectifier) is not a suitable digital signal due to the finite time constants in the rectifier. The purpose of the demodulator is to recover a logic-level (rail to rail) signal from the rectifier output. The demodulator inputs are the rectifier output and a low-pass-filtered version of the rectifier output. The low-pass filter has an approximately 16 kHz bandwidth to filter out the negative pulses.

The demodulator schematic is shown in Fig. 8. The first stage provides differential to single-ended conversion. The second stage significantly boosts the signal swing in order to achieve logic level voltages. Thick-oxide buffers with a low supply voltage (0.7 V) prevent crowbar current that could result from the limited slew rate of the low-power comparator. The differential pair is biased with 75 nA, and the common-source stage is biased with 300 nA which only draws current when the reader carrier is on. The unity gain bandwidth of demodulator is set to 2 MHz. This ensures reliable recovery of the input

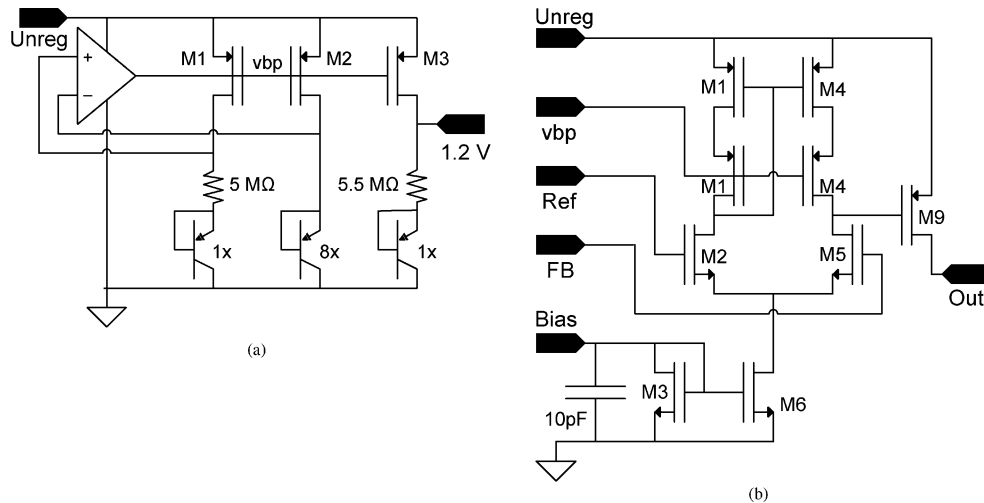


Fig. 6. Bias voltage and supply generation schematics. (a) Bandgap reference schematic. (b) Voltage regulator schematic.

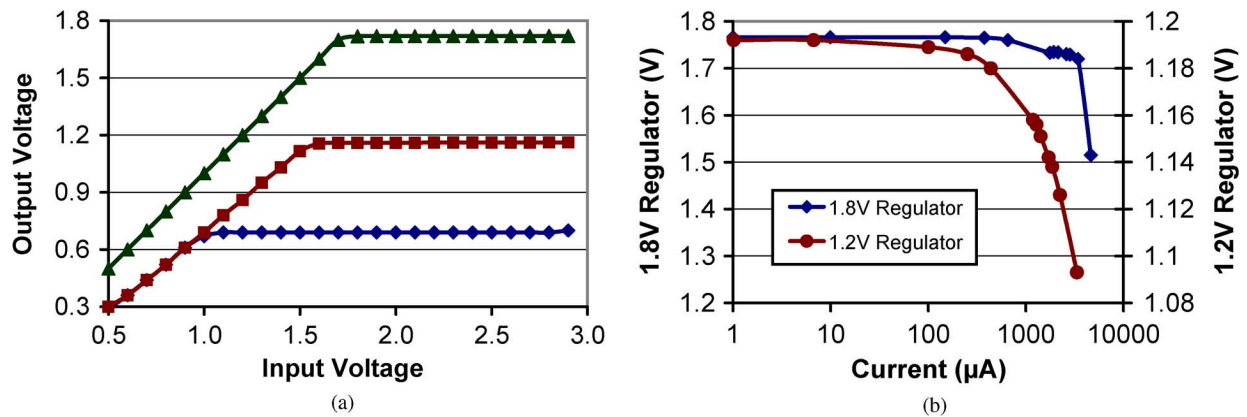


Fig. 7. Measured regulator performance. (a) Line regulation for the 1.8 V (top), 1.2 V (middle) and 0.7 V (bottom) regulators. (b) Load regulation.

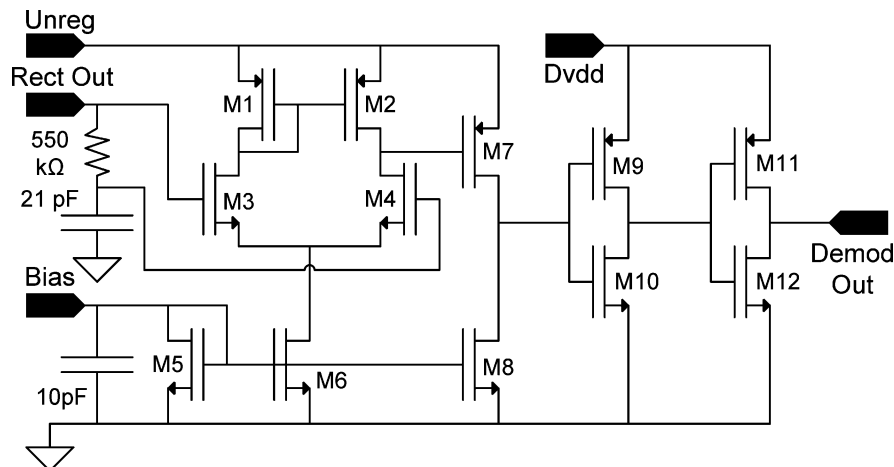


Fig. 8. Analog demodulator that is used to recover a logic-level baseband signal from the rectifier output.

signal (up to 1.2 MHz) under a wide range of temperature and process corners.

E. Modulator

RFID tags communicate with the interrogator by either absorbing or reflecting the RF carrier sent by the interrogator. A

single transistor switch is used to modulate the tag reflection coefficient. A thick-oxide (IO) high- V_t device is used to prevent breakdown when the tag is near the reader (at which point greater than 10 dBm can be expected at the tag antenna). Experimental results demonstrate that the tag is downlink limited, and the return loss with the modulator enabled is -0.6 dB.

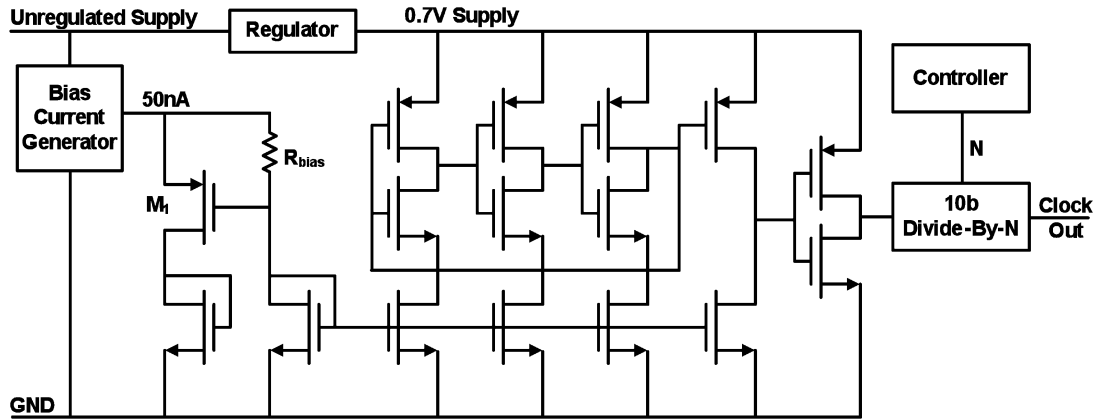


Fig. 9. Three-stage ring oscillator schematic and prescale divider.

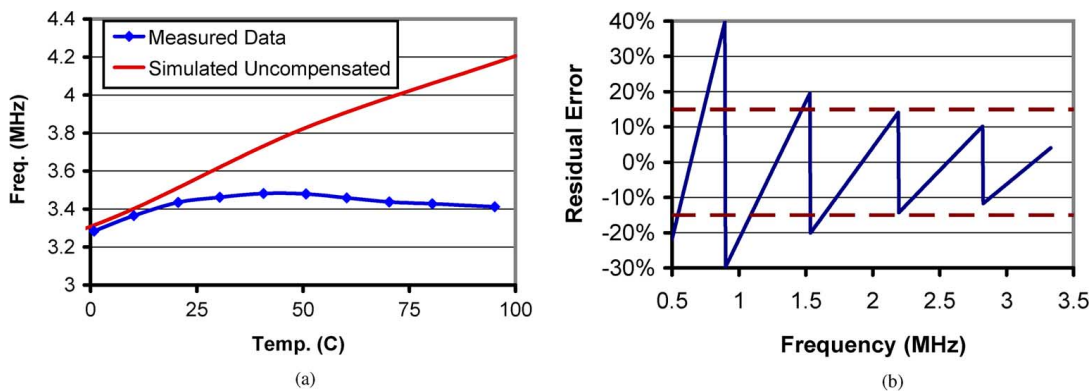


Fig. 10. Oscillator performance versus temperature and divider operation. The red dashed lines denote the acceptable residual error as per the EPC specification. (a) Measured and simulated oscillator frequency versus temperature. (b) Divider output residual error versus input (oscillator) frequency.

F. Oscillator

Many tags use a 1.5 MHz clock, which requires the tag oscillator PVT stability to meet Gen2 timing specifications ($\pm 15\%$ for 640 kHz uplink) as the integer divider residual exceeds the allotted tolerance. Resistor trimming [4], bias current tuning [3], phase locking, and quartz references have been proposed to compensate for PVT variation but are prohibitive due to cost, power and size constraints. We propose a 3 MHz temperature-stabilized ring oscillator, shown in Fig. 9, which lowers the divider residual such that PVT compensation can be performed by the integer divider. The oscillator consumes 260 nA from the 0.7 V digital supply. We take three approaches to improve stability. First, large device size and careful layout limit process variation to 13% (measured, Fig. 10(a)). Second, the divider residual is centered at zero, which reduces the peak residual by a factor of 2 (Fig. 10). Third, a novel temperature compensation shown in Fig. 9 tunes the oscillator bias current by measuring and compensating the V_t temperature coefficient. As temperature decreases, f_{osc} decreases. The negative $\Delta V_{gs}/\Delta T$ coefficient increases the current through R_{bias} , providing the oscillator increased current to compensate for the temperature variation. Careful design of the transistor inversion coefficient and value of R_{bias} , results in a first-order temperature coefficient cancellation.

G. ADC

An 8-bit successive-approximation register (SAR) ADC digitizes the amplified biosignals. Virtually no static current is consumed through the use of a discrete-time comparator. Complete testing and characterization of the ADC is presented in [18].

H. Unique ID Generation

In order to associate sensor data from a tag with the object that the tag is attached to, the tag must have a unique ID. Traditionally, the tag is manually programmed with a specified ID by the interrogator, which is stored in a non-volatile memory (NVM) such as flash, EEPROM, or resistor fuse array. However, these NVM require large voltages and currents, which in turn degrade tag performance due to increased power consumption. We instead employ lithographic uncertainty and random dopant fluctuation to create a unique, random ID for each tag [17]. Specifically, the tag reads the power-on state of a 128-bit SRAM array. This technique allows reliable identification of ICs without explicit programming steps. On average, 95% of the bits are stable, and unstable bits are easily filtered out via application-level software. Note that unstable ID bits do not impair Gen2 protocol compatibility due to the use of random numbers as tag handles.

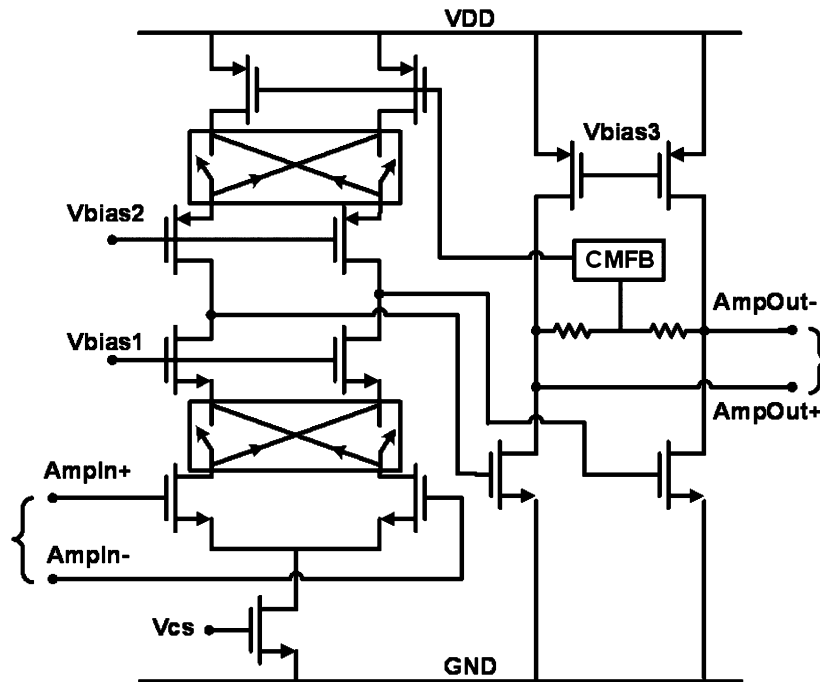


Fig. 11. Schematic of fully-differential chopper-stabilized low-noise amplifier. Compensation capacitors and nulling resistors are not included for simplicity.

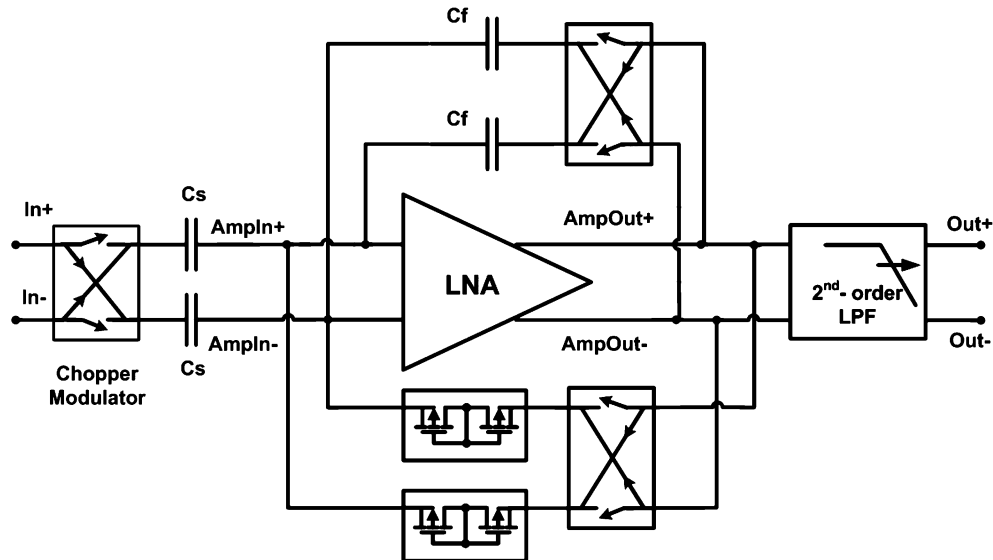


Fig. 12. Chopper amplifier architecture.

V. BIOSIGNAL AMPLIFIER

A. Chopper-Stabilized Low-Noise Amplifier Design

Our multi-purpose sensing tag is designed for a variety of sensor interfaces, including biosignal detection, thermocouple readout, and gas detection. These applications demand an extremely low noise floor ($< 2 \mu\text{V}_{\text{RMS}}$ input referred) under a relatively low bandwidth ($< 1 \text{ kHz}$). When the signals of interest fall below a few hundred Hertz, the dominating circuit noises shift from the thermal noise to $1/f$ and popcorn noise [19]. Excess low-frequency noise can undermine the system's signal-to-noise ratio (SNR) and cause errors in the measurement. As a result, we use a chopper-stabilized topology to suppress $1/f$ noise and offset that plague sub-micron CMOS processes.

Closed-loop chopper-stabilization has been adopted recently [20], [21], [19] to suppress gain and sensitivity errors, as well as to prevent saturation due to amplifier offset. Among the recent implementations, [19] provides the best figure-of-merit so far. AC feedback is employed to ensure all signals entering the amplifier are well above $1/f$ noise corner. However, separate active input-biasing circuitry is used, and higher supply voltage is required due to single-ended approach.

As shown in Figs. 11 and 12, we employ a fully-differential closed-loop architecture to ensure sufficient linearity and supply rejection. Operating transistors in the subthreshold region enables the use of a power-efficient telescopic-cascode op-amp topology under low supply voltages. Signal up-conversion occurs at the gate of the input transistors, which are biased in weak inversion to maximize the transconductance. We introduce a

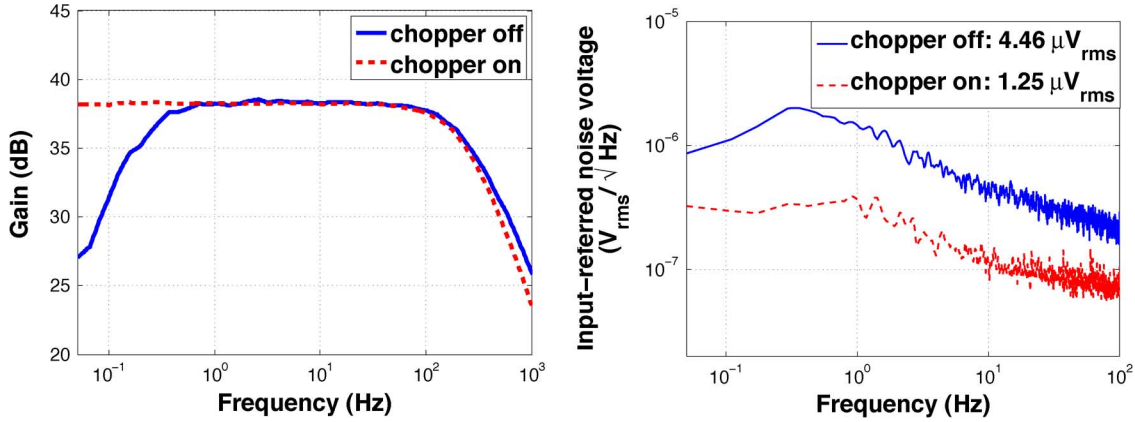


Fig. 13. Measured transfer function and noise plot of the low-noise chopper-stabilized biosignal amplifier. (a) Chopper-Amplifier Gain Magnitude Plot, (b) Chopper-Amplifier Noise Plot.

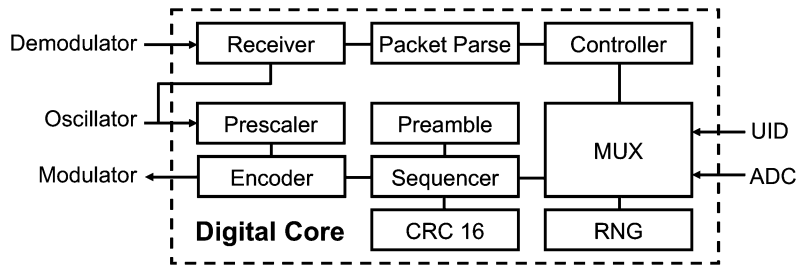


Fig. 14. EPC Gen2 digital core with sensor data interface.

novel dual-feedback technique to simultaneously set the mid-band gain of the amplifier through C_{fb} , and bias the amplifier's input node through high-resistance pseudo-resistors. Chopper switches are included in both the signal and biasing paths to not only guarantee negative feedback around the amplifier, but also avoid using additional input-biasing circuitry as in [19]. We realize the chopper modulator with a minimally-sized CMOS transmission gate to minimize charge injection. The input capacitance (C_{in}) is 15 pF. When modulated with a 10 kHz chopper clock, the input impedance ($1.06\text{ M}\Omega$) is high enough to avoid loading the electrodes for biomedical applications. The ratio of C_{in} and C_{fb} establishes a 40 dB midband gain. C_{fb} is sized slightly smaller (140 fF) to take into account the addition of parasitic and switch capacitances.

Two additional sets of chopper switches are added in the first stage of the amplifier: one set of switches is placed at the drains of the input transistors to demodulate the ac signal down to baseband and modulate the input offsets up to the chopper frequency; another pair is placed at the drains of the pMOS current source to modulate their flicker noise up to a higher frequency. At the output of the amplifier, the signal returns to baseband while the offsets and flicker noise are modulated up to high frequency and then filtered by the amplifier's second stage. The second stage is implemented as common-source to increase the output swing under low supply voltages. The output is then fed back to the summing node at the input of the amplifier after being modulated up to the chopper frequency. In order to avoid large passive devices, we implemented continuous-time tunable Gm-C filters to reduce ripple at the output of the amplifier. The input-referred noise from the ripple filter (Gm-C filters) is designed to be negli-

gible. The six achievable bandwidths of the Gm-C filters are logarithmically spread between 150 Hz to 400 Hz. The tunability of the filters is realized through digital control of the transconductor current.

B. Low-Noise Amplifier Measurement Results

Fig. 13(a) plots the gain magnitude with chopping on and off. The midband gain for both cases is approximately 38.5 dB. When the chopper clock is off, the amplifier operates as a conventional AC-coupled amplifier and has a high-pass corner of 0.2 Hz. Amplification is preserved down to DC when chopper-stabilization is enabled. The tunable low-pass corner is set to 230 Hz in this measurement.

Fig. 13(b) illustrates the input-referred noise of the amplifier with chopping on and off. Low frequency spot noise is reduced by more than a decade when the chopper is enabled. The measured integrated noise from 0.05 Hz to 100 Hz is $1.25\ \mu\text{V}_{\text{rms}}$ when the chopper switches are on, compared to $4.46\ \mu\text{V}_{\text{rms}}$ when the chopper switches are off.

VI. DIGITAL CORE

A high level block diagram of the digital core is shown in Fig. 14. The *Receive* block performs clock and data recovery (CDR) on the PIE signal. A *Packet Parse* block decodes EPC commands and stores relevant information for the *Controller* and *Prescaler*. The *Controller* block decides what packet to send after receiving a packet from the reader, and enables the transmitter logic if appropriate. The *Sequencer* constructs an

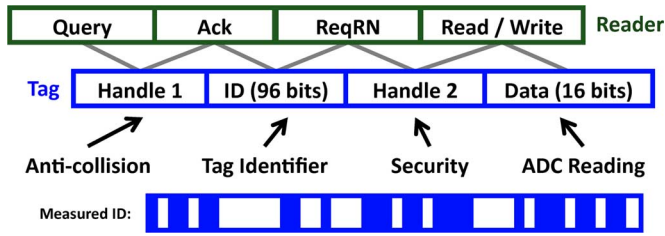


Fig. 15. EPC Gen2-compliant sensor data protocol.

TABLE II
SENSOR TAG PERFORMANCE

System:	
Current Consumption	9.2 μ A
Unregulated Voltage	1.8 V - 3.6 V
RF Sensitivity	-12 dBm
Peak Rectifier Efficiency	37%
IC Area	2.0mm ²
Components:	
Analog Core	1.2 μ A
Reference Oscillator	260 nA
Digital Core	6.0 μ A
ADC & UID	500 nA
Biosignal Amp	1.2 μ A

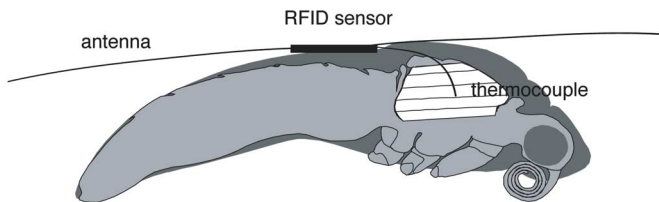


Fig. 16. Schematic of the cross section of *Manduca* dorsolongitudinal muscle temperature measurement.

EPC-compliant packet including preamble and CRC, and the *Encoder* converts the data bit stream to Miller or FM0 encoding.

VII. SENSOR DATA PROTOCOL

Interoperability with COTS readers requires Gen2 protocol compatibility. Fig. 15 illustrates how the protocol works and how sensor data is retrieved. The Query and ReqRN commands implement anticollision in the protocol. These commands require random numbers, which are generated by sampling the (unpredictable) clock phase at the downlink baseband edges and passing it through an LFSR. The tag identifier (ID) is queried via the Ack command, and the ID is generated by the UID, as described in Section IV.H. Finally, sensor data is returned through the Read command. An example measured ID returned by one of our tags is shown in Fig. 15.

VIII. PERFORMANCE

This system was fabricated in a 0.13 μ m CMOS process. The die photo is shown in Fig. 19. A ground shield made of the 4- μ m-thick top aluminum metal covers the entire die to reduce the impact of EMI, capacitive, and light sensitivity on the extremely high impedance internal instrumentation nodes. First-silicon functionality was ensured through extensive FPGA testing of the digital core with a commercial RFID reader through a passive RFID analog front end composed of

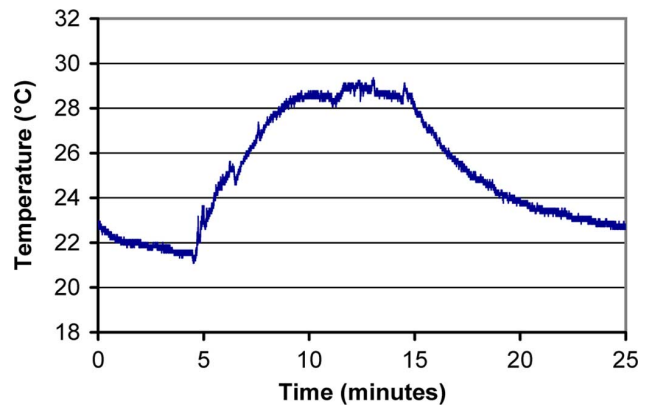


Fig. 17. Measured temperature versus time from a tethered moth.

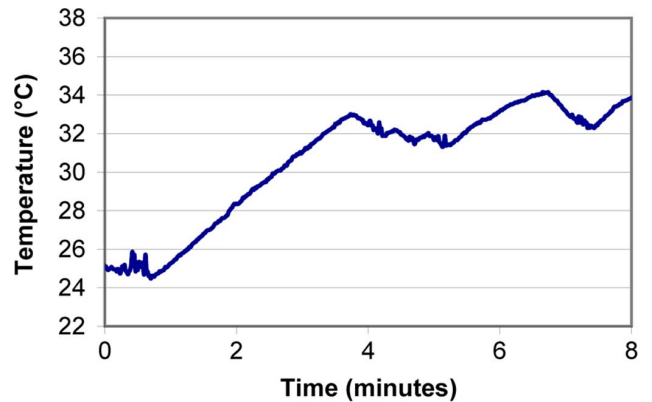


Fig. 18. Measured temperature versus time from an untethered moth.

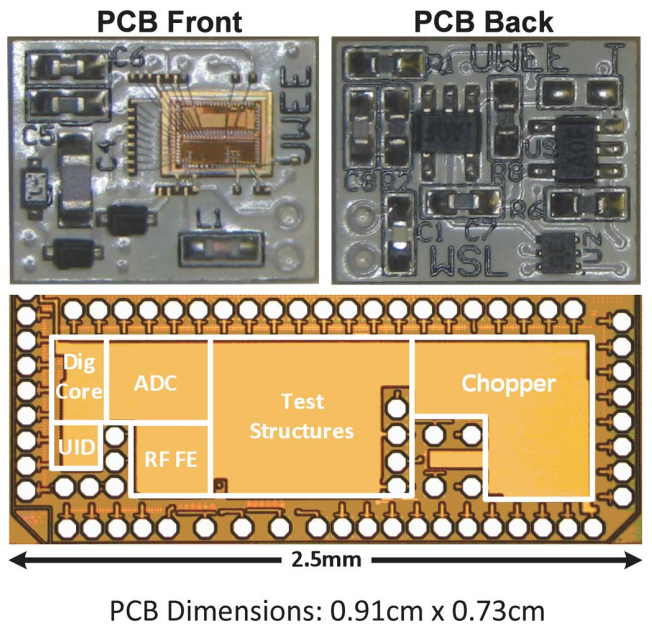


Fig. 19. Chip and board micrographs.

discrete COTS ICs (see [2] for a schematic). Mixed signal simulations were performed to verify the communication interfaces between the digital core and the analog blocks (UID, ADC, and demodulator).

Table II compares the performance of this work to other tags presented in the literature. For a comparison of tag features,



Fig. 20. Photograph showing an untethered moth with the RFID measurement sensor.

refer back to Table I. This work compares favorably to other sensor tags without resorting to duty cycling [2], [22], loss of Gen2 compatibility [23], or elimination of the ADC [24]. Drawing comparisons to tags lacking sensors and/or addressability (all remaining tags) is less meaningful, but [1] and [25] clearly achieve the best RF sensitivity for a fully-passive tag. In part, our use of a linear regulator, ADC and more complex state machine simply limit the achievable sensitivity.

IX. IN VIVO, IN-FLIGHT BIOSIGNAL ACQUISITION

The ability to monitor *in vivo* biosignals such as temperature and motor patterns in an organism without altering the kinematic output is invaluable to many fields of biology, and is particularly important in understanding the control of movement in humans and other animals. Currently, there is only a general understanding of how temperature affects muscle performance. Though the temperature dependence of muscle contraction has already been established from *in vitro* preparations, the ability to correlate locomotor and kinematic performance with body temperature has thus far been hindered by obtrusive sensors [26], [27].

The hawkmoth, *Manduca sexta*, provides a well-documented model system in which to develop an understanding between biosignal output and behavior. Like other endotherms, *Manduca* utilizes the heat released from synchronous isometric muscle contractions to generate an elevated core temperature [28]. Increased muscle temperature allows these insects to increase their wing beat frequency and thus produce greater mechanical power output [29].

We used our sensing tag with a COTS RFID reader to record the in-flight temperature of the dominant flight muscles of *Manduca* (the dorsolongitudinal muscles: DLM₁ *sensu* [30]). The copper-constantan thermocouple was inserted into the DLM₁, approximately 3 mm below the dorsal aspect of the cuticle (Fig. 16). Using the instantaneous read-out of our wireless sensor, we can correlate the rate of heat production during flight

TABLE III
COMPARISON OF PUBLISHED (MEASURED) TAG PERFORMANCE

Author	Sensitivity	Active	Sleep	Tech.	Clock
This Work	-12dBm	9 μ A	6 μ A	0.13 μ	3MHz
Sample [2]	-9dBm ^a	800 μ A	2 μ A	PCB	3MHz
Kim [24]	-5.3dBm ^b	15 μ A	0.5 μ A	0.25 μ ^c	-
Kocer [22]	-12.3dBm ^a	660 μ A	0.9 μ A	0.25 μ	-
Nakamoto [32]	-6.2dBm ^d	87.8 μ W	-	0.25 μ	-
Pillai [33]	19dBm ^a	12 μ A	0.6 μ A	1.0 μ	-
Karthauss [1]	-17.8dBm	1.5 μ A	-	0.5 μ ^c	300kHz
Barnett [25]	-14dBm	2.75 μ A ^b	-	0.13 μ ^c	1.28MHz
Shen [23]	-8.2dBm ^b	10.2 μ A ^e	-	0.35 μ ^c	-
Cho [34]	-12.9dBm ^b	3.4 μ A	-	0.25 μ	330kHz
Shenghua [35]	-20.5dBm ^b	0.9 μ W	-	0.18 μ	-

^aDuty cycling required at this input power.

^bCalculated based on 20% rectifier efficiency and 50% modulation losses.

^cProcess includes Schottky diodes.

^dNo power numbers reported, but authors claim 36.6% rectifier efficiency and 4.3m range given 4W EIRP.

^eSimulation result, no measurements reported.

TABLE IV
RFID SENSOR SPECIFICATIONS

Sample Rate	100 Hz
Resolution	4.7 μ V / 0.11 $^{\circ}$ C
Peak Noise	\pm 1.5 bits = \pm 7 μ V

with the observed kinematic response. Both rapid and large scale changes in body temperature will reveal how *Manduca* thermoregulates according to its energetic requirements.

Results from tethered and untethered temperature measurements show that the temperature of the DLM₁ increased with time, stabilizing around 29 $^{\circ}$ C for the tethered moth and 30–35 $^{\circ}$ C for the untethered moth (Figs. 17 and 18). Because the behavior of the moth is uncontrolled, the untethered data show the moth resting at the 4 minute and 7 minute time marks. The tethered data represent one continued period of activity by

the moth. The temperature is different between the two trials due to different implant depths of the thermocouple as well as different characteristics of the moth.

Fig. 19 shows the PCB used for this experiment, which measures less than 1 cm² and weighs 0.25 g. Additional thermocouple gain is achieved using on-board 1.8 V micropower opamps that are powered from our on-chip 1.8 V regulators. A photograph of the moth wearing the system is shown in Fig. 20. Including the antenna and thermocouple, the entire system weighs 0.35 g. Full system specifications are listed in Table IV. The power of our moth-worn system is two orders of magnitude lower than an active radio-based tag [31]. This work enables the first long-term in-flight recording of an insect by removing both the wires and batteries from the recording equipment.

X. CONCLUSION

For many wirelessly-deployed sensors, periodic battery replacement is costly at best and infeasible at worst. Two key features of RFID make it attractive for wireless sensor deployment: power is wirelessly and deliberately supplied to the tag, and backscatter modulation allows for nearly-zero power tag-to-reader communication. Coupling this technology with biomedical applications promises exciting advances in medical delivery. Specifically, Gen2 compatibility, tag addressability, and the ability to interface with useful sensors will enable these biosensors to be deployed as medical and research tools.

Our multi-purpose sensing tag was designed for a variety of sensor interfaces such as such as EMG (electromyograms), thermocouple readout, and gas detection. These applications demand an extremely low noise floor ($< 2 \mu\text{V}_{\text{rms}}$ input referred) under a relatively low bandwidth ($< 1 \text{ kHz}$). Furthermore, the tag lifespan should not be limited by battery life. This paper demonstrates the feasibility of *in vivo*, untethered, in-flight temperature recording of insects. The key novelty is that this long-term wireless recording was previously unattainable due to the size, weight, and lifespan of conventional sensors.

REFERENCES

- [1] U. Karthaus and M. Fischer, "Fully integrated passive UHF RFID transponder IC with 16.7- μW minimum RF input power," *IEEE J. Solid-State Circuits*, vol. 38, no. 10, pp. 1602–1608, Oct. 2003.
- [2] A. P. Sample, D. J. Yeager, P. S. Powledge, A. V. Mamishev, and J. R. Smith, "Design of an RFID-based battery-free programmable sensing platform," *IEEE Trans. Instrumentation and Measurement*, vol. 57, no. 11, pp. 2608–2615, Nov. 2008.
- [3] F. Cilek, K. Seemann, D. Brenk, J. Essel, J. Heidrich, R. Weigel, and G. Holweg, "Ultra low power oscillator for UHF RFID transponder," in *Proc. 2008 IEEE Int. Frequency Control Symp.*, May 2008, pp. 418–421.
- [4] R. Barnett and J. Liu, "A 0.8 V 1.52 MHz MSVC relaxation oscillator with inverted mirror feedback reference for UHF RFID," in *Proc. IEEE Custom Integrated Circuits Conf. (CICC'06)*, Sep. 2006, pp. 769–772.
- [5] C. Klappf, A. Missoni, W. Pribyl, G. Holweg, and G. Hofer, "Analyses and design of low power clock generators for RFID TAGs," in *Research in Microelectronics and Electronics 2008 (PRIME 2008)*, Apr. 2008, pp. 181–184.
- [6] F. Song, J. Yin, H. Liao, and R. Huang, "Ultra-low-power clock generation circuit for EPC standard UHF RFID transponders," *Electronics Lett.*, vol. 44, no. 3, pp. 199–201, 2008, 31.
- [7] I. Zalvide, J. Vicario, and I. Velez, "Power and energy optimization of the digital core of a Gen2 long range full passive RFID sensor tag," in *Proc. 2008 IEEE Int. Conf. RFID*, Apr. 2008, pp. 125–133.
- [8] A. Ricci, M. Grisanti, I. De Munari, and P. Ciampolini, "Design of a 2 μW RFID baseband processor featuring an AES cryptography primitive," in *Proc. 15th IEEE Int. Conf. Electronics, Circuits and Systems (ICECS 2008)*, Sep. 2008, pp. 376–379.
- [9] T. Umeda, H. Yoshida, S. Sekine, Y. Fujita, T. Suzuki, and S. Otaka, "A 950 MHz rectifier circuit for sensor networks with 10 m-distance," in *2005 IEEE Int. Solid-State Circuits Conf. (ISSCC) Dig. Tech. Papers*, Feb. 2005, vol. 1, pp. 256–259.
- [10] G. De Vita and G. Iannaccone, "Design criteria for the RF section of UHF and microwave passive RFID transponders," *IEEE Trans. Microwave Theory Tech.*, vol. 53, no. 9, pp. 2978–2990, Sep. 2005.
- [11] R. Barnett, S. Lazar, and J. Liu, "Design of multistage rectifiers with low-cost impedance matching for passive RFID tags," in *2006 IEEE Radio Frequency Integrated Circuits (RFIC) Symp. Dig. Papers*, Jun. 2006, p. 4.
- [12] J. Yi, W.-H. Ki, and C.-Y. Tsui, "Analysis and design strategy of UHF micro-power CMOS rectifiers for micro-sensor and RFID applications," *IEEE Trans. Circuits Syst. I: Reg. Papers*, vol. 54, no. 1, pp. 153–166, Jan. 2007.
- [13] S. Mandal and R. Sarpeshkar, "Low-power CMOS rectifier design for RFID applications," *IEEE Trans. Circuits Syst. I: Reg. Papers*, vol. 54, no. 6, pp. 1177–1188, Jun. 2007.
- [14] H. Nakamoto, D. Yamazaki, T. Yamamoto, H. Kurata, S. Yamada, K. Mukaida, T. Ninomiya, T. Ohkawa, S. Masui, and K. Gotoh, "A passive UHF RFID tag LSI with 36.6% efficiency CMOS-only rectifier and current-mode demodulator in 0.35 μm FeRAM technology," in *2006 IEEE Int. Solid-State Circuits Conf. (ISSCC) Dig. Tech. Papers*, Feb. 2006, pp. 1201–1210.
- [15] T. Le, K. Mayaram, and T. Fiez, "Efficient far-field radio frequency energy harvesting for passively powered sensor networks," *IEEE J. Solid-State Circuits*, vol. 43, no. 5, pp. 1287–1302, May 2008.
- [16] R. Glidden, C. Bockorick, S. Cooper, C. Diorio, D. Dressler, V. Gutnik, C. Hagen, D. Hara, T. Hass, T. Humes, J. Hyde, R. Oliver, O. Onen, A. Pesavento, K. Sundstrom, and M. Thomas, "Design of ultra-low-cost UHF RFID tags for supply chain applications," *IEEE Commun. Mag.*, vol. 42, no. 8, pp. 140–151, Aug. 2004.
- [17] Y. Su, J. Holleman, and B. Otis, "A digital 1.6 pJ/bit chip identification circuit using process variations," *IEEE J. Solid-State Circuits*, vol. 43, no. 1, pp. 69–77, Jan. 2008.
- [18] J. Holleman, A. Mishra, C. Diorio, and B. Otis, "A micro-power neural spike detector and feature extractor in 13 μm CMOS," in *Proc. IEEE Custom Integrated Circuits Conf. (CICC 2008)*, 2008, pp. 333–336.
- [19] T. Denison, K. Consoer, W. Santa, A. Avestruz, J. Cooley, and A. Kelly, "A 2 μW 100nV/ $\sqrt{\text{Hz}}$ chopper-stabilized instrumentation amplifier for chronic measurement of neural field potentials," *IEEE J. Solid-State Circuits*, vol. 42, no. 12, pp. 2934–2945, Dec. 2007.
- [20] K. Makinw and J. Huijsing, "A wind sensor with an integrated low-offset instrumentation amplifier," in *Proc. 8th IEEE Int. Conf. Electronics, Circuits and Systems (ICECS 2001)*, 2001, pp. 1505–1508.
- [21] R. Yazicioglu, P. Merken, R. Puers, and C. Van Hoof, "A 60 μW 60nV/ $\sqrt{\text{Hz}}$ readout front-end for portable biopotential acquisition systems," *IEEE J. Solid-State Circuits*, vol. 42, no. 5, pp. 1100–1110, May 2007.
- [22] F. Kocer and M. Flynn, "A new transponder architecture with on-chip ADC for long-range telemetry applications," *IEEE J. Solid-State Circuits*, vol. 41, no. 5, pp. 1142–1148, May 2006.
- [23] H. Shen, L. Li, and Y. Zhou, "Fully integrated passive UHF RFID tag with temperature sensor for environment monitoring," in *Proc. 7th Int. Conf. ASIC (ASICON'07)*, Oct. 2007, pp. 360–363.
- [24] S. Kim, J.-H. Cho, H.-S. Kim, H. Kim, H.-B. Kang, and S.-K. Hong, "An EPC Gen2 compatible passive/semi-active UHF RFID transponder with embedded FeRAM and temperature sensor," in *Proc. IEEE Asian Solid-State Circuits Conf. (ASSCC'07)*, Nov. 2007, pp. 135–138.
- [25] R. Barnett, G. Balachandran, S. Lazar, B. Kramer, G. Konnail, S. Rajasekhar, and V. Drobny, "A passive UHF RFID transponder for EPC Gen2 with -14 dBm sensitivity in 0.13 μm CMOS," in *2007 IEEE Int. Solid-State Circuits Conf. (ISSCC) Dig. Tech. Papers*, Feb. 2007, pp. 582–623.
- [26] A. Bennett, "Thermal dependence of muscle function," *Amer. J. Physiol.—Regulatory, Integrative and Comparative Physiology*, vol. 247, no. 2, p. 217, 1984.
- [27] R. Josephson, "Contraction dynamics of flight and stridulatory muscles of Tettigoniid insects," *J. Experiment. Biol.*, vol. 108, no. 1, p. 77, 1984.
- [28] B. Heinrich, "Thermoregulation in endothermic insects," *Science*, vol. 185, no. 4153, p. 747, 1974.

- [29] R. Stevenson and R. Josephson, "Effects of operating frequency and temperature on mechanical power output from moth flight muscle," *J. Experiment. Biol.*, vol. 149, no. 1, p. 61, 1990.
- [30] Y. Kondoh and Y. Obara, "Anatomy of motoneurons innervating mesothoracic indirect flight muscles in the silkworm, *Bombyx mori*," *J. Experiment. Biol.*, vol. 98, no. 1, p. 23, 1982.
- [31] D. Daly, P. Mercier, M. Bhardwaj, A. Stone, Z. Aldworth, T. Daniel, J. Voldman, J. Hildebrand, and A. Chandrakasan, "A pulsed UWB receiver SoC for insect motion control," *IEEE J. Solid-State Circuits*, vol. 45, no. 1, p. 153, Jan. 2010.
- [32] H. Nakamoto, D. Yamazaki, T. Yamamoto, H. Kurata, S. Yamada, K. Mukaida, T. Ninomiya, T. Ohkawa, S. Masui, and K. Gotoh, "A passive UHF RF identification CMOS tag IC using ferroelectric RAM in 0.35- μ m technology," *IEEE J. Solid-State Circuits*, vol. 42, no. 1, pp. 101–110, Jan. 2007.
- [33] V. Pillai, H. Heinrich, D. Dieska, P. Nikitin, R. Martinez, and K. Rao, "An ultra-low-power long range battery/passive RFID tag for UHF and microwave bands with a current consumption of 700 nA at 1.5 V," *IEEE Trans. Circuits Syst. I: Reg. Papers*, vol. 54, no. 7, pp. 1500–1512, Jul. 2007.
- [34] N. Cho, S.-J. Song, S. Kim, S. Kim, and H.-J. Yoo, "A 5.1- μ W UHF RFID tag chip integrated with sensors for wireless environmental monitoring," in *Proc. 31st European Solid-State Circuits Conf. (ESSCIRC 2005)*, Sep. 2005, pp. 279–282.
- [35] Z. Shenghua and W. Nanjian, "A novel ultra low power temperature sensor for UHF RFID tag chip," in *Proc. IEEE Asian Solid-State Circuits Conf. (ASSCC'07)*, Nov. 2007, pp. 464–467.



Daniel J. Yeager (S'05) received the B.S. degree (*cum laude*) and the M.S. degree in electrical engineering from the University of Washington, Seattle. He is currently working toward the Ph.D. degree in electrical engineering at the University of California at Berkeley.

During 2007, he worked at Intel Research Seattle, developing a programmable passive RFID tag that is now used by over 30 research groups to study novel RFID applications. He has published in a broad range of RFID topics including encryption, neural and EEG

brain recording, strain measurement for aircraft and buildings, capacitive user interfaces, and battery-free data logging. His research interests include wireless sensing and energy scavenging, especially for biomedical applications.

Mr. Yeager's work is supported by the National Science Defense and Engineering Grant.



Fan Zhang (S'08) received the B.S. degree in electrical engineering and computer sciences from the University of California at Berkeley in 2007, and the M.S. degree in electrical engineering from the University of Washington, Seattle, in 2009. She is currently working toward the Ph.D. degree.

From 2006 to 2007, she interned at Agilent Technologies, Santa Clara, CA. In 2009, she interned at Intel Corporation, Hillsboro, OR, and worked on modeling of sigma-delta phase-locked loops. Her current research interests include low-power analog

and RF circuit design for biomedical applications.

Ms. Zhang was a corecipient of the 2010 DAC/ISSCC Student Design Contest Award.



Azin Zarrasvand received the B.S.E.E. degree from the Iran University of Science and Technology, Tehran, Iran, in 1999, and the M.S.E.E. degree from the University of Washington, Seattle, in 2009.

Her interests are in low-power circuits and systems. She has recently joined the Microelectronics Department at Raytheon Corporation, Andover, MA.



Nicole T. George received the Bachelor's degree in biology from the University of California at Berkeley in 2006. She is currently pursuing the Ph.D. degree in the Department of Biology at the University of Washington, Seattle.

Her research currently focuses on the mechanical and functional consequences of temperature gradients within insect flight muscle.

Ms. George's work is supported by the NSF Graduate Research Fellowship Program. She is a member of the Society for Integrative and Comparative Bi-

ology and the Biophysical Society.



Thomas Daniel received the M.S. degree in biology from the University of Wisconsin in 1978 and the Ph.D. degree in biology from Duke University in 1982.

From 1982 to 1984, he was the Bantrell Fellow in Engineering Sciences at the California Institute of Technology. Since then, he has been on the faculty in Biology at the University of Washington, Seattle, where he served as its inaugural chair during 2001–2008. He is also Adjunct Professor in the Department of Bioengineering and a Professor in the

University of Washington Graduate Neurobiology and Behavior. His research focuses on the control and dynamics of animal locomotion.



Brian P. Otis (S'96–M'05–SM'10) received the B.S. degree in electrical engineering from the University of Washington, Seattle, and the M.S. and Ph.D. degrees in electrical engineering from the University of California at Berkeley.

He joined the faculty of the University of Washington as Assistant Professor of Electrical Engineering in 2005. His primary research interests are ultra-low-power RFIC design and bioelectrical interface circuits and systems. He previously held positions at Intel Corp. and Agilent Technologies.

Dr. Otis served as an Associate Editor of the IEEE TRANSACTIONS ON CIRCUITS AND SYSTEMS PART II. He received the U.C. Berkeley Seven Rosen Funds Award for innovation in 2003, was a corecipient of the 2002 ISSCC Jack Raper Award for an Outstanding Technology Directions Paper, and a recipient of the National Science Foundation CAREER Award in 2009.